Check for updates

Photophysical and biological assessment of coumarin-6 loaded polymeric nanoparticles as a cancer imaging agent†

Yiota Gregoriou, [iD] *[ab] Gregoria Gregoriou,[b] Andreas Manoli,[cd] Paris Papageorgis,[cd] Benedict Mc Larney, [iD] [e] Despoina Vangeli,[f] Sarah McColman, [iD] [g] Vural Yilmaz, [iD] [b] Hsiao-ting Hsu,[a] Magdalena Skubal,[e] Anuja Ogirala,[a] Evangelia Athanasiou, [iD] [ch] David T. Cramb, [iD] [g] Nikolas Dietis,[f] Katerina Strati, [iD] [b] Grigorios Itskos,[cd] Andreas I. Constantinou[b] and Chrysafis Andreou [iD] *[ch]

Polymeric nanoparticles can prove beneficial in oncology as they sidestep limitations associated with traditional small-molecule pharmaceuticals. With respect to drug delivery, polymeric nanoparticles possess structural features that make them suitable as carriers for therapy and imaging contrast, as their core/shell morphology offers an effective method of transport that provides increased tumor access with reduced side effects, especially for drugs with low water solubility. Herein, we present a polymeric nanoparticle made from pluronic F127 and vitamin E-TPGS encapsulating coumarin-6 for the optical imaging of cancer. We explored the biophysical properties of the construct using an array of optical and physical techniques, evaluated its uptake in breast cancer cell lines, the *in vivo* toxicokinetics in zebrafish, and its biodistribution profile in mouse xenograft models bearing PC3 tumors overexpressing the prostate-specific membrane antigen (PSMA). The biophysical characterization of the nanoformulation, combined with its selective uptake by cancer cells, its low *in vivo* toxicity profile, and effective tumor targeting demonstrate the versatility and potential of this nanoparticle formulation for drug delivery applications.

Introduction

Drug delivery vehicles in the nanoscale offer an ideal platform for selective tissue targeting and theranostic applications, delivering treatment and imaging contrast agents to pathological loci.[1-3] Particularly for the optical imaging of cancer, conventional contrast agents lack tissue specificity and can lead to off-target toxicity.[4] Additionally, many effective contrast agents exhibit poor aqueous solubility leading to low bioavailability and suboptimal detection

capabilities. The utilization of nanodrug delivery vehicles as contrast agents for cancer applications has attracted great interest as it offers significant benefits, sidestepping limitations associated with traditional formulations.[5] Nanovehicles provide an innovative method of drug transport that offers protection from degradation, increases drug solubility, extends circulation time, delays drug clearance, and enhances tumor access *via* the enhanced permeability and retention (EPR) effect.[6,7]

Polymeric nanoparticles have gained attention as cancer drug delivery vehicles due to their unique structural features but also due to the biocompatibility and biodegradability exhibited by the constituent polymers.[8] Amphiphilic polymers in aqueous solutions self-assemble into micellar structures with a hydrophilic shell and a hydrophobic core. The shell provides solubility to the micelle and can aid in avoiding opsonization when in circulation; the core serves as cargo space for hydrophobic anticancer drugs or imaging contrast agents, facilitating delivery to the target. Herein, we present a polymeric micelle formulation encapsulating coumarin-6 (C6), as a model lipophilic contrast agent for optical imaging. The nanoconstruct was made from pluronic F127 and vitamin E-TPGS, based on our previous work.[9] C6 is a synthetic derivative of coumarin, a naturally occurring

[a] *Memorial Sloan Kettering Cancer Center, New York, NY, USA*
[b] *Department of Biological Sciences, University of Cyprus, Nicosia, Cyprus. E-mail: gregoriou.panayiota@ucy.ac.cy*
[c] *Emphasis Research Centre, University of Cyprus, Nicosia, Cyprus*
[d] *Department of Physics, University of Cyprus, Nicosia, Cyprus*
[e] *Molecular Pharmacology Program, Memorial Sloan Kettering, New York, NY, USA*
[f] *Medical School, University of Cyprus, Nicosia, Cyprus*
[g] *Department of Chemistry and Biology, Toronto Metropolitan (Ryerson) University, Toronto, ON, Canada*
[h] *Department of Electrical and Computer Engineering, University of Cyprus, Nicosia, Cyprus. E-mail: andreou.chrysafis@ucy.ac.cy*
† Electronic supplementary information (ESI) available. See DOI: https://doi.org/10.1039/d3sd00065f

phenolic compound. Coumarin derivatives have been reported to bestow a variety of beneficial effects, acting as anticoagulants, anticonvulsants, and antioxidants;[10,11] importantly, coumarins have been used preclinically in cancer research due to their potent anticancer activity.[12–17] Additionally, photo-activatable coumarin derivatives have been incorporated into nanoparticles as a mechanism for on-demand drug release.[18,19]

In an attempt to explore the feasibility of clinical translation of the C6-loaded nanoparticle (C6-NP), we explored the biophysical properties of the nanoformulation with different optical and physical techniques. Additionally, we evaluated its toxicity and biodistribution in zebrafish, and explored the C6-NP uptake in breast cancer cell lines. Moreover, we evaluated the nanoformulation's biodistribution profile in mouse xenograft models inoculated with PC3 cells, overexpressing the prostate specific membrane antigen (PSMA), as a model for human prostate cancer.

Experimental

Details regarding the synthesis and characterization of nanoparticles are available in the "Materials and methods" section of the ESI.† These include the materials and reagents used, physical characterization with atomic force microscopy (AFM) and dynamic light scattering (DLS), chemical determination of the drug-loading efficiency, measurement of pH-dependent drug release, and photophysical characterization using photoluminescence and fluorescence correlation spectroscopy (FCS). Additionally, *in vitro* experiments are described, related to fluorescence imaging in cell cultures, and flow cytometry analysis, as well as experimental details related to the breeding and housing of zebrafish.

In vivo experiments

Zebrafish housing and breeding. Zebrafish (*Danio rerio*; WIK strain) were used in this study, maintained at a dedicated zebrafish facility licensed by the Veterinary Services of the Ministry of Agriculture, Rural Development and Environment of Cyprus of the Republic of Cyprus (license CY/EXP/PR.L8/2018). All procedures regarding animal housing, maintenance, and breeding were carried out as described in the ESI,† following an established protocol.[20]

Zebrafish larvae C6-NP exposure. A total of 16 zebrafish larvae, at 15 days past fertilization, were used for the pilot exposure experiments. After the morning feeding, the larvae were placed in a 96-well sterile plate at one larva per well in 200 μl system water for two hours, before randomization in two equal groups (treatment and control). In the treatment group, the water was replaced with 200 μl of 1 mg ml⁻¹ C6-NPs diluted in fresh system water and in the control group the water was replaced with 200 μl of fresh system water. The larvae were left for 24 hours in the plate at 28 °C with no other intervention. At 24 hours, the larvae were 'washed' three times to remove any potential externally-attached compound, by placing them in a 6-well sterile plate with fresh water, at one larva per well, for two minutes per wash. The larvae were then transferred in a new 96-well plate at one larva per well to perform whole-well fluorescence measurements at peak excitation/emission wavelengths (Ex: 460 nm, Em: 530 nm) using an ultrasensitive multimodal microplate reader with monochromator/filter combination optics (Spark 20 M, Tecan, Switzerland) at prior-optimized reader settings (30 flashes; 40 μs integration time; 10 μs lag time; 50 ms settle time; 75 gain; 25 000 μm 3D lens Z-position). A larvae health-assessment was then conducted by morphological observational screening using a standard stereoscope (*i.e.*, body size and shape, eye morphology and movement, pigmentation, tail morphology). At the last stage, the larvae re-entered a new two-step wash cycle with fresh system water for two minutes each, prior to commencing a second fluorescent measurement at 30 hours post-exposure, using the same parameters as the first.

Adult zebrafish C6-NP exposure. A total of 21 adult zebrafish (1 year old; male) were used to determine the overall toxicity and organ biodistribution of C6 administration. After the morning feeding, the fish were randomized in two groups (treatment and control), before measuring their total weight using a sensitive scale (weight ranging between 0.9–1 g). All fish were first anesthetized by individual immersion in beaker with 0.0168% MS-222 for 3–5 minutes (ref. 21) until complete loss of reaction to external stimuli. The fish were then transferred on a suitably formed moist sponge with their head facing outward to allow administration *via* oral-gavage. The treatment group (*n* = 15) received 10 μl of a 0.01 mg ml⁻¹ C6-NP solution by the oral-gavage method[22] using a micropipette, whereas the control group (*n* = 6) received 10 μl of fresh system water. After treatment, each fish was placed individually in a beaker with 100 ml fresh system water until full recovery from anesthesia and return of normal activity. The fish were then transferred to individual tanks (single-housed) and fed. A second treatment was given after 96 hours following the same protocol and methods. Fish survival and vital health indicators were monitored for a total of 144 hours after the first treatment. During the monitoring period, the fish were fed twice every twenty-four hours.

After the end of the monitoring period, all fish were euthanized by individual immersion in a beaker with 0.2% MS-222 for 10 minutes (ref. 23) until complete loss of opercular movement and absent breathing movements. The fish were then decapitated on the bench before being dissected under a stereoscope. Five organs (heart, brain, swim bladder, and stomach with intestines) were removed from all fish, and placed separately in an appropriate lysis buffer (digestion buffer G2, QIAGEN, 800 mM quinidine: HCl, 5% Tween-20, 0.5% Triton X-100, 30 mM EDTA, pH 8.0). The tissues in lysis buffer were sonicated in a water-bath sonicator for 25 minutes and vortexed for 5 minutes. The lysates were centrifuged for 10 minutes at 12 000*g* and then 200 μl of supernatant were transferred into a clear 96-well plate for fluorescence measurements. Water, lysis buffer, and

a pure C6-NP solution were used as controls. Fluorescence measurements followed the same settings and protocol as in the larvae exposure measurements.

Mouse model. All mouse handling, housing, imaging, and surgery were performed in accordance with Institutional Animal Care and Use Committee (IACUC) guidelines at MSKCC and the NIH Guide for the Care and Use of Laboratory Animals. To induce the xenograft model, 4–6 weeks male NOD.Cg-*Prkdc*^{scid}/J mice (Jackson Laboratory) were injected on the flank with 5×10^6 PC3-PSMA cells. Anesthesia was induced *via* 3% isoflurane in 100% O$_2$ v/v followed by 1–2% isoflurane in 100% O$_2$ v/v for maintenance. The mice ($n = 4$) were injected with C6-NPs 4 weeks after tumor inoculation when the tumors reached a volume approximately of 200 mm^3. Different nanoparticle formulations were administered *via* tail-vein injection, to evaluate the effective dose and quantitative response of the C6-NPs. Control mice with the same tumor model ($n = 3$) were injected with PBS. Fluorescent imaging was performed on an IVIS® (Spectrum CT, Perkin Elmer) at time points of 1, 4, and 24 hours after C6-NP administration with excitation at 465 nm and emission at 580 nm, lamp setting of high, 0.15 s exposure time, binning of 8, f-stop 2. Euthanasia was performed using CO$_2$ in accordance with approved protocols. The mice were dissected and the excised organs imaged *ex vivo*. The same settings were used for both *in vivo* and *ex vivo* imaging of mice and excised organs.

Results and discussion

Photophysical characterization

Physical properties. The size, morphology, and zeta potential of the nanoparticles were analyzed by AFM and DLS. The size distribution was found to be bimodal by both methods. AFM showed nanoparticles of circular structure with sizes of 22 nm and 65 nm, respectively, as shown in Fig. 1A. The size distribution profile determined by DLS (Fig. 1B) was similarly bimodal, with two distinct populations observed with sizes of 18 nm and 126 nm, with a polydispersity index of 0.26. The smaller size observed *via* the AFM is attributed to the drying up of the sample and spreading on the grid, as opposed to the fully hydrated suspended nanoparticles measured by DLS. This may also indicate that the nanoparticles release their hydrophobic load when they are plated on the flat substrate for imaging. The zeta potential was measured as −19.86 mV, which is considered moderately anionic and is likely stable in solution,[24] as higher repulsive interaction between the nanoparticles results in higher stability and a more uniform size distribution.[25]

Encapsulation efficiency. Percentage drug encapsulation efficiency (% EE) was calculated by absorbance spectrometry, with two approaches: directly, from the absorbance of the C6 that was encapsulated in the micelle; and indirectly, based on the supernatant collected from the washes during synthesis, corresponding to the C6 that was not encapsulated. The direct method found the encapsulation
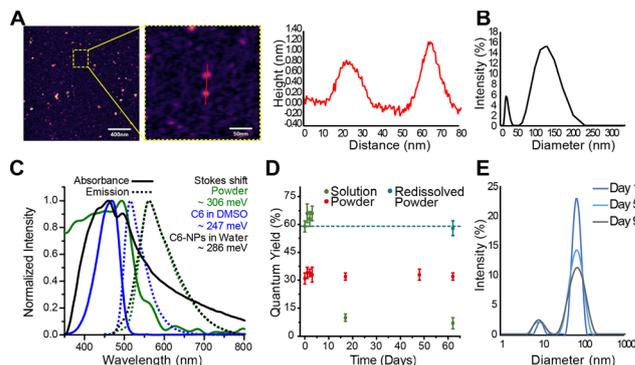

Fig. 1 Photophysical characterization. (A) Evaluation of nanoparticle size and morphology. Representative AFM micrographs of the nanoparticle deposited on mica pretreated with 3-aminoprophy-trietoxy silane (3-APTES). Height *versus* distance analysis of two representative nanoparticles as seen in the magnified AFM image. (B) DLS measurement of C6-NPs in DI water shows a bimodal distribution. (C) Photoluminescence properties of pure C6 in DMSO (blue), C6-NPs in powder form (green) and C6-NPs in water (black). The absorption spectra appear in solid lines and the emission spectra in dotted lines. (D) Quantum yield over a period of 62 days for the C6-NPs in solution (green) and the C6-NPs in powder form (in red). The samples were stored at room temperature in between measurements. The sample in powder form from day 62 was resuspended in water and the QY was recorded and can be seen in blue. (E) DLS measurement shows the mean size of the nanoparticles in saline solution at 37 °C over a period of nine days after preparation. No major size changes were observed in the period over which the nanoparticle was monitored. Abbreviations: AFM: atomic force microscopy and DLS: dynamic light scattering.

efficiency to be 81.18% ± 3.94%, and the indirect method, similarly, 74.55% ± 2.77%. The high encapsulation efficiency observed suggests that the nanoparticle preparation method used allows for high drug loading.

Drug release. The amount of C6 released from the nanoparticles was measured under three different pH conditions (pH 7.3, 6.0, and 4.5) to mimic the progressively acidic environment the C6-NPs can encounter, from physiological conditions, to the tumor microenvironment, and finally the lysosome. Lower pH values were found to cause faster release of the dye, in agreement with previous reports of pluronic-F127-based nanoparticles,[26] however the increase was not pronounced. The time-release response is shown in Fig. S1.†

Photoluminescence. The optical properties of pure C6 and C6-NPs were investigated in powder form and relevant solvents (in DMSO and deionized water) and are recorded in Fig. 1C. For C6 measurements in water, C6 powder was first dissolved in DMSO and further diluted in DI water. The absorption and emission maxima of the nanoparticle were 460 nm and 550 nm, respectively. These parameters were used to record nanoparticle fluorescence in all relevant studies following.

PL stability. The optical properties of the C6-NP in powder form and in solution were monitored over a period of 62 days (Fig. S2†). The absorption profile of the nanoparticle in water suggests that the formulation is stable for several days but

fails by day 18. The increase in absorbance observed on day 62 may suggest the release of C6 from the nanoparticle in the solution. This is further supported by the increasing absorbance peak at 460 nm due to C6, over time. This peak is not visible on day 0 (Fig. S3†) as C6 is fully encapsulated within the micelle. Similarly, in the PL study the fluorescence intensity drops, and the peak flattens after day 18. This may suggest that the C6 that leached out of the nanoparticle degraded by this time point (past day 18) or even agglomerated in solution leading to quenching. Additionally, the absorbance profile of the nanoparticle in powder form suggests a change in composition past day 3. A second peak starts to form at 460 nm which suggests the presence of water. This implies that the nanoparticle absorbed water in storage possibly due to moisture in the air. The PL spectra for the nanoparticle in powder form, show a reduction in fluorescence from day 0 to day 3 suggesting possible oxidation of coumarin that had leached out of the nanoparticle due to the presence of moisture in the sample.

Moreover, the QY profile of the nanoparticle in solution and in powder form was studied over a period of 62 days. As can be seen in Fig. 1D, a small increase in QY is seen from day 0 to 3 suggesting the release of C6 from the nanoparticle into the solution. In the powder form, the QY remains constant for the duration of the study suggesting no further degradation of the nanoparticle under the storage conditions studied (room temperature and sealed on slide). To further justify this statement, we redissolved the powder sample from day 62 in water and measured the QY. The QY was the same as that of the nanoparticle in water on day 0, further suggesting the chemical stability of the powder. On the contrary, the QY of the C6-NPs in water past day 3 decreases suggesting changes in composition. These could be either chemical changes (*i.e.*, oxidation) or physical changes (*i.e.*, aggregation), both of which cause quenching of the fluorescence. The quantum yield of C6 dissolved in DMSO was measured as 74 ± 5%, in agreement with previous reports.[27,28] The lower quantum yield measured for the C6-NPs is likely due to interactions (π-stacking) of the dye molecules packed in close proximity within the nanoparticle.

NP stability in saline. The stability of the nanoparticle in saline was of interest to enable reliable *in vivo* studies. The nanoparticles were dispersed in saline and the size was monitored by DLS over a period of nine days. Between measurements, the samples were kept in a 37 °C incubator to mimic physiological conditions. Size measurements were performed on day 1, 5, and 9 after preparation. Overall, as shown in Fig. 1E, we did not observe any significant size changes in the period mentioned indicative of nanoparticle composition changes.

C6-NP size and stability in relevant media by FCS. The C6-NPs were suspended in PBS with 5% fetal bovine serum. Preliminary FCS experiments indicated that the nanoparticle solution comprised of two components: a larger, slower-diffusing component, and a smaller, faster-diffusing component. This was observed by examining the shape of the

autocorrelation curves, noting two clear decay times (Fig. S4†). Using a two-component model to fit the data (as detailed in the ESI†) resulted in a reduced chi-squared value for the fit decreasing by an order of magnitude, and an increased R^2 value, suggesting a better fit to the data. This further supports the bimodal size distribution shown by DLS and AFM analysis.

Additionally, hydrodynamic diameters determined by FCS for either component in solution did not change notably during the three hour timespan over which the samples were measured for all replicates (Fig. S5†). Large fit errors and high data scatter due to large fluorescence events (*i.e.* bright particles) fluctuating in the focal volume and skewing the fits prohibits confident stability conclusions from being drawn from these size data. To confirm relative stability over a three-hour window, $G(0)$ values for both components were also plotted against time as a way to track changes in composition over this time period. No notable trends were observed for either component, and relatively small error bars give stability conclusions from these data sets higher reliability (Fig. S6†).

In vitro characterization

Fluorescence microscopy. To qualitatively assess the uptake of nanoparticles, the MCF10CA1a-Luc (MIV-luc)[29] cell line was used as a model breast cancer cell line. As a first test for possible nanoparticle uptake, MIV-luc is a good choice because it shows no autofluorescence in the green (coumarin-6) channel. The cells were incubated with 250 μg ml^{-1} C6-NPs for 4 h. The fluorescent images, as seen in Fig. 2A, clearly indicate nanoparticle uptake into the cytoplasm at 4 h of incubation. Once uptake was confirmed further quantitative uptake assays were performed using the flow cytometry on additional breast cancer cell lines. No toxicity effects were observed on the cells during imaging, in agreement with previous reports that C6 presents very low toxicity.[30–32] The polymeric nanoparticles used here have also been previously reported to have no toxic effects.[9]

Flow cytometry. Nanoparticle uptake was evaluated by flow cytometry as presented in Fig. 2B. We used three cancer cell lines (MDA-MB-231, MCF-7, MIV-luc), and a non-malignant breast epithelial cell line (MCF-10A). MDA-MB-231 and MCF-7 represent different cancer phenotypes, as MCF-7 are hormone dependent while MDA-MB-231 are triple negative. Cells were incubated with 100, 250 and 500 μg ml^{-1} of C6-NPs for 30, 60 and 240 minutes. The concentrations shown are based on nanoparticle weight and correspond to approximately 25, 50 and 125 μg ml^{-1} of coumarin-6, respectively. Drug concentrations were calculated based on the % EE previously determined, and the amount of coumarin-6 used during synthesis. Measurements were performed in triplicate for all cell lines except for MIV-luc (n = 1), with similar results. Following nanoparticle treatment, the uptake clearly increases in a time and dose dependent manner, as seen in Fig. 2C, for all breast cancer cell lines
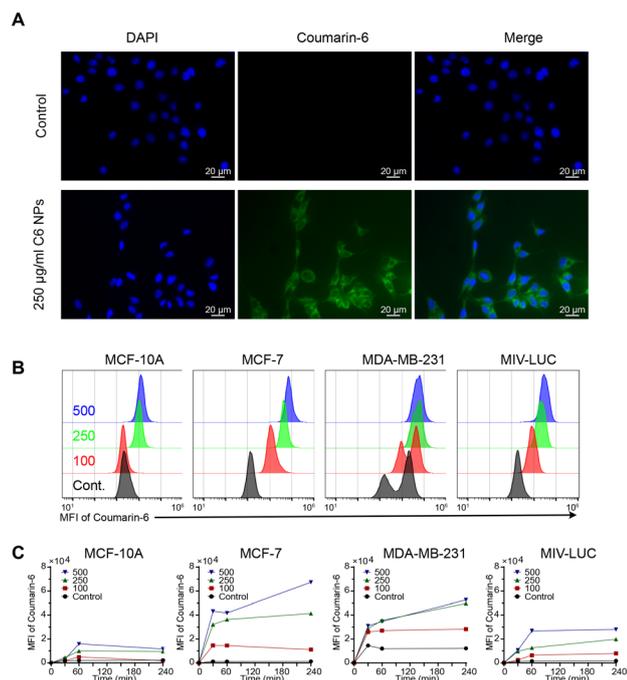
Fig. 2 Cellular uptake. (A) Fluorescence microscopy of cells treated with C6-NPs. Blue represents nuclear staining (DAPI) and green represents C6. MIV-luc cells were incubated with 250 μg ml^{-1} of C6-NPs for 240 minutes. Green fluorescence was observed in the cytoplasm suggesting nanoparticle uptake. Scale bar: 20 μm. (B and C) Dose dependent cellular uptake of C6-NPs analysed by flow cytometry. MCF-10A, MCF-7, MDA-MB-231, and MIV-luc cells were seeded in 6-well plates (2 × 10^5 per well) and incubated with 100, 250 and 500 μg ml^{-1} of C6-NPs for 30, 60 and 240 min. (B) Representative histograms showing the MFI of all cell lines at the 240 minute time point treated with 500 μg ml^{-1} (blue), 250 μg ml^{-1} (green) and 100 μg ml^{-1} (red) C6-NPs. No-NP controls are shown in black. (C) Time response uptake curves of MCF-10A, MCF-7, MDA-MB-231, and MIV-luc cell lines treated with 500 μg ml^{-1} (blue), 250 μg ml^{-1} (green) and 100 μg ml^{-1} (red) C6-NPs. No-NP controls are shown in black. Results are represented as MFI values for a set of measurements. Data were analyzed using GraphPad Prism version 8.0.0 for Windows, GraphPad software, San Diego, California USA. Abbreviation: mean fluorescence intensity (MFI).

used and most importantly the uptake in cancer cell lines was more effective in comparison to the immortalized non-cancer breast cell line, MCF-10A. This specificity could be meaningful in targeted theranostic applications in oncology. Additionally, of importance is the successful uptake in MDA-MB-231, a very hard to treat triple-negative cell line, due to the absence of expression of recognized therapeutic targets.

In vivo studies

Zebrafish toxicity and kinetics. Zebrafish larvae were used as a pilot model for the assessment of C6-NP toxicity and kinetics, prior adult exposure. As shown in Fig. 3A, the C6-NP-treated larvae showed significantly higher fluorescence than the non-treated control group immediately after 24 hours of exposure (**** $p < 0.0001$, One-Way ANOVA with
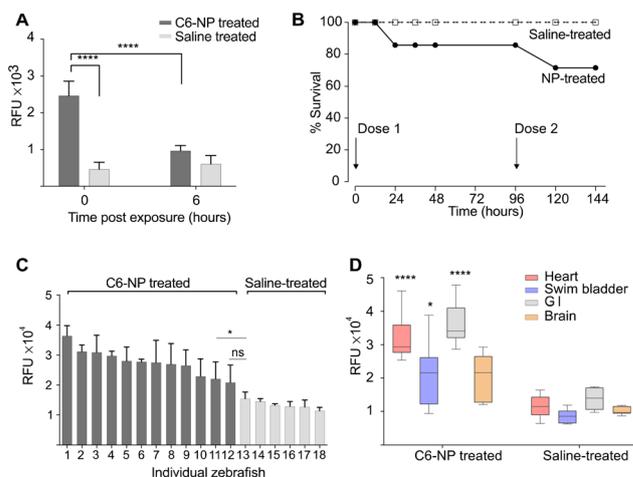

Fig. 3 Uptake assessment in zebrafish. (A) Fluorescence measurement of larvae after 24 h of exposure to C6-NP, at 0 and 6 hours post-exposure. The C6-NP-treated larvae showed significantly higher fluorescence after 24 h of exposure than their non-treated counterparts (2.47 ± 1.10 vs. 0.46 ± 0.10; **** $p < 0.0001$ by one-way ANOVA with Bonferroni correction). The C6-NP-treated animals showed significant loss of fluorescence at 6 h post-exposure (0.61 ± 0.20) compared to the paired 0-h measurement (**** $p < 0.0001$ by one-way ANOVA with Bonferroni correction). Data are presented as RFU × 10^3 mean ± SEM. (B) Kaplan–Meier survival analysis of C6-NP-treated and saline-treated adult zebrafish for 144 hours after the first dose. A log-rank test (Mantel–Cox) and a Gehan–Breslow–Wilcoxon test showed no significant difference in the % survival between the two groups (chi-square 1.405 and $p = 0.236$; chi-square 1.402 and $p = 0.236$). (C) The total fluorescence of four extracted organs (heart, swim bladder, brain and stomach/intestines; GI) from each adult zebrafish that survived in the C6-NP-treated and saline-treated groups, presented in descending order. The C6-NP-treated group showed collectively significant difference in fluorescence compared to saline-treated group (3.04 ± 1.2 vs. 1.38 ± 0.98; $p < 0.0001$ by Student's t-test). All C6-NP-treated animals but one (12) showed significant difference in fluorescence, with p-values ranging from 0.0296 (* animal 11) to 0.0008 (one-way ANOVA with Sidak correction compared to animal 13). Data are presented as RFU × 10^4 mean ± SEM. (D) Fluorescence exhibited in four major organs between C6-NP-treated and saline-treated adult zebrafish. All organs from C6-NP-treated animals showed significantly higher fluorescence than their counterparts from the saline-treated animals (one-way ANOVA with Sidak correction; **** $p < 0.0001$, *** $p < 0.0004$, * $p < 0.05$).

Bonferroni correction) suggesting significant absorption and distribution of C6-NP in the larvae body. The fluorescence of the C6-NP-treated larvae dropped significantly 6 hours later (**** $p < 0.0001$, one-way ANOVA with Bonferroni correction), indicating significant excretion/elimination of the nanoparticle within 6 hours. Most importantly, no mortality occurred in the larvae in both groups up to 30 hours of monitoring and there were no distinct morphological observations of the exposed larvae compared to control (data not shown). This suggests that exposure of zebrafish larvae with 200 μl of 1 mg ml^{-1} C6-NP has no lethality and does not exhibit an obvious systemic toxicity at least until 30 hours post-exposure.

To study the toxicokinetics of C6-NPs in adult zebrafish, a Kaplan–Meier survival analysis for the total duration of the

study (144 hours after first dose) was conducted with an output of survival percentage based on the number of each group (Fig. 3B). In the treatment group, two fish died at the 48 hour checkpoint and one fish died at the 120 hour after the first dose. No fish died in the control group. Comparison tests of the survival of two groups were performed using a log-rank (Mantel–Cox) test (chi-square: 1.405; $p = 0.236$) and a Gehan–Breslow–Wilcoxon test (chi-square: 1.402; $p = 0.236$). All tests showed no significant difference in survival between the two groups. All treated fish that survived at 144 hours post-exposure did not exhibit changes in their monitored health indicators (data not shown).

The C6-NP biodistribution in four major organs (heart, brain, swim bladder and stomach/intestines) of the treated adult zebrafish was measured at 144 h after the first dose of C6-NP. The fluorescence exhibited from the four organs of each individual fish was measured, reflecting the overall distribution of C6-NP in these organs per animal (Fig. 3C). The C6-NP-treated animals showed considerable inter-variability of the C6-NP biodistribution in their organs, ranging from a mean of 3.65 (animal 1) to 2.18 RFU $\times 10^4$ (animal 12). Fig. 3C presents this variability in descending order of the organ-exhibited fluorescence of the animals. The last C6-NP-treated animal in sequence (12) showed no significant difference in its organs' fluorescence compared to the first-in-order saline-treated animal (13), whereas all other C6-NP-treated animals showed a significant difference, with p-values from 0.0296 (* animal 11) to 0.0008 (by one-way ANOVA with Sidak's correction – all compared to animal 13). When comparing the collective exhibited fluorescence between the two groups, by type of organ (Fig. 3D), each type-group of organs from C6-NP-treated animals showed significantly higher fluorescence than its respective type in saline-treated animals (one-way ANOVA with Sidak's correction), with the heart and the stomach/intestines (GI) showing the highest difference (**** $p < 0.0001$).

Imaging tumors in mice. Male NOD.Cg-*Prkdc*^{scid}/J mice inoculated with a PC3-PSMA cells were used as models for human prostate cancer to measure nanoparticle accumulation and retention in the tumor as well as off target nanoparticle delivery. The mice were injected *via* the tail vein with C6-NPs for imaging and biodistribution analysis. The tumor volume was monitored, and the mice were injected when the tumors reached a size of about 200 mm^3 and appeared to be fast growing.

We studied 4 different nanoparticle doses to determine how concentration changes alter tumor accumulation and off-target effects. The first formulation was a 10 mg ml^{-1} nanoparticle solution in saline that was not filtered prior to injection. DLS analysis (data not shown) revealed a polydisperse solution with aggregates up to a few micrometers. The second formulation was a filtered version of the first (10 mg ml^{-1} nanoparticle solution) through a 450 nm syringe filter to remove aggregates. The third and fourth formulations were further diluted by 2× and 4×, respectively. DLS analysis on the filtered solutions confirmed the absence
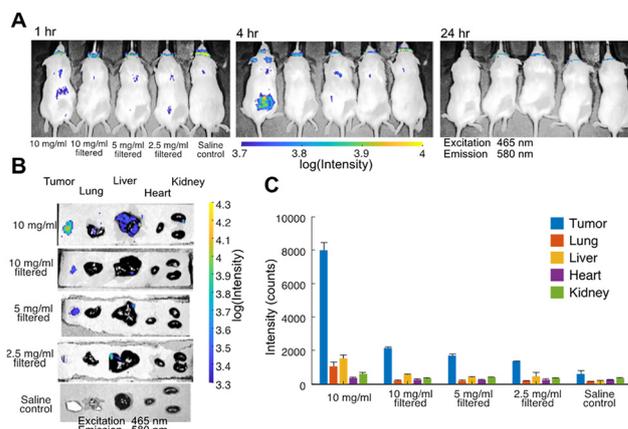

Fig. 4 Biodistribution of nanoparticles in representative mice bearing PC3-PSMA tumors. Different C6-NP formulations were delivered *via* a single tail vein injection: 10 mg ml^{-1} unfiltered; 10 mg ml^{-1} filtered; 5 mg ml^{-1} filtered; 2.5 mg ml^{-1} filtered; no NP control. (A) Mice were imaged using the IVIS® at 0 h, 4 h and 24 h post injection. C6 fluorescence was detected in the tumor through the skin only for the highest injected dose. (B) At 24 h post injection, mice were sacrificed, and tumors and major organs were harvested for *ex vivo* imaging. The fluorescent signal was detected in all tumors of animals injected with C6-NPs. Liver and lung off-target delivery was also observed, although at markedly lower intensities than to the tumor. (C) Bar chart showing the mean fluorescence intensity for each dose and the control, in the tumor, lung, liver, heart, and kidneys. Error bars denote standard deviation within each region.

of micrometer range particulates. Saline solution, free of nanoparticles, was used as a control. C6-NP tumor accumulation was monitored for all the formulations by detecting the fluorescence *in vivo* on an IVIS® at 0 h, 4 h, and 24 h after injection. As shown in Fig. 4A, fluorescence at the tumor was detected through the skin at 4 h after injection for the first (unfiltered) formulation. The fluorescence was not detectable at 24 h, as the nanoparticle entered deeper into the tumor vasculature and was obscured by the skin. The fluorescence at the tumor was not detectable in mice receiving the other formulations at any time point as the concentration was too low to be detected through the skin. At 24 h after injection all mice were sacrificed, and major organs were dissected for further imaging. More specifically the tumor, lung, liver, heart, and kidneys from all mice (including the control) were imaged on the IVIS®, as shown in Fig. 4B. Tumor accumulation was detected in all tumors from injected mice, with the fluorescence signal progressively diminishing as the injected C6-NP concentration decreased, as shown in Fig. 4C. Markedly lower fluorescence was seen in the control. Although the unfiltered formulation exhibited the highest fluorescence signal in the tumor it also exhibited higher liver and lung accumulation, possibly due to the larger size of the injected nanoparticles, which facilitates sequestration from circulation by the reticuloendothelial system.[33] By filtering out the larger particles off-target delivery is less pronounced.

As the C6-NPs did not feature any moieties for specific molecular targeting, accumulation in the tumor is attributed

mainly to the EPR effect.[7] Additionally, the ability of Pluronic block copolymers to induce changes in the microviscosity of cell membranes[34,35] may explain the high tumor selectivity and little off-target effect observed. These alterations in membrane structure are more pronounced in cancerous cells compared to healthy cells. Furthermore, membrane fluidization in cancerous cells causes inhibition of the P-glycoprotein efflux function.[36] This may lead to a synergistic effect, as vitamin E TPGS is known to do the same.[37] Collectively, these results demonstrate promising tumor targeting. The formulation that had the highest concentration and contained larger nanoparticles exhibited the most effective tumor accumulation but also the most off target effect, particularly liver uptake. Taking these results into consideration the filtered formulation, at high concentration is deemed the most effective.

Conclusions

The C6-loaded polymeric nanoparticles presented in this study demonstrate an effective platform for the delivery of therapeutic agents and imaging contrasts.

Our results from FCS, DLS and AFM showed that the formulation's size distribution was bimodal. Two distinct, spherical populations were observed with sizes (as reported by DLS) of 18 nm and 126 nm, with adequate stability in solution. The % EE of C6 loaded was calculated *via* two methods and found to be around 75–80%, suggesting successful loading efficacy of the drug by the preparation method used.

The stability of the formulation in various forms (powder and in solution) and within relevant media was also investigated. Quantum yield data showed that the C6 within the nanoparticle retained a stable signal at room temperature for more than 2 months in powder form and up to 3 days in water. Moreover, data from FCS suggested that the nanoparticles remained stable during the three hour timespan over which the samples were measured in PBS and FBS, with no signs of aggregation. The stability of the nanoparticle in saline at 37 °C was also investigated by DLS and the results suggested structural stability of the nanoparticle up to 9 days after preparation.

The nanoparticles demonstrated uptake in cancer cell lines. The time and dose-dependent uptake profile was measured in breast cancer cell lines, MDA-MB-231, MCF-7 and MIV-luc and compared to a non-malignant breast epithelial cell line (MCF-10A), as the control. Our results suggested that nanoparticle uptake displayed high selectivity towards the cancer cell lines, in a dose and time-dependent manner, with minimal uptake in the control.

Additionally, we showed successful nanoparticle oral absorption, distribution, and excretion in zebrafish. A time-dependent toxicity assessment after C6-NP exposure on zebrafish revealed no mortality in larvae up to 6 h after a 24 h exposure and 17% mortality rate in adult zebrafish up to 144 h after exposure, indicating that further investigation may be needed.

Moreover, preliminary experiments in mouse models bearing a PC3 tumor xenograft overexpressing PSMA showed successful delivery of the nanoparticle to the tumor. Off-target delivery, particularly in the liver and lungs, was more prominent when the formulation used contained large aggregates, compared to the filtered formulation containing smaller nanoparticles. Although the fluorescence signal of C6 was seen in the excised tumors, non-invasive imaging through the skin was not possible for all but the highest injected dose, due to the high absorbance and scattering of optical frequencies by biological tissues. A fluorescent dye excited and emitting in the infrared is likely to have better performance than C6 when delivered *via* the polymeric micelles described in our study.

Author contributions

Y. G. attained funding for this work, designed all experiments presented in this work, executed all experiments relating to C6-NP synthesis and physicochemical characterization (*in vitro* and *in vivo*), analyzed and interpreted all results and drafted the manuscript. G. G. performed all *in vitro* experiments (fluorescence imaging, flow cytometry, cell culture maintenance) helped with data analysis and C6-NP synthesis and edited the manuscript. A. M., P. P. and E. A. executed and analyzed all experiments relating to NP photoluminescence and stability. B. M., C. H., M. S. and A. O. assisted with the mouse experiments. D. V. and N. D. designed, executed and analyzed all *in vivo* zebrafish experiments. S. M. and D. T. C. executed and analyzed all FCS experiments. V. Y. helped in the acquisition and analysis of the flow cytometry experiments. A. I. C. first proposed the idea of making TPGS nanoparticles. K. S. and G. I. edited the manuscript. C. A. performed data analysis, helped in the preparation of figures, and edited the manuscript.

Conflicts of interest

The authors have declared that no competing interest exists.

Acknowledgements

Notes and references

1 Y. Yao, Y. Zhou, L. Liu, Y. Xu, Q. Chen, Y. Wang, S. Wu, Y. Deng, J. Zhang and A. Shao, Nanoparticle-Based Drug Delivery in Cancer Therapy and Its Role in Overcoming Drug Resistance, *Front. Mol. Biosci.*, 2020, **7**, 193.

2 Y. Dang and J. Guan, Nanoparticle-based drug delivery systems for cancer therapy, *Smart Mater. Med.*, 2020, **1**, 10–19.

3 C. Andreou, S. Pal, L. Rotter, J. Yang and M. F. Kircher, Molecular Imaging in Nanotechnology and Theranostics, *Mol. Imaging Biol.*, 2017, **19**(3), 363–372.

4 L. Smith, Z. Kuncic, K. Ostrikov and S. Kumar, Nanoparticles in Cancer Imaging and Therapy, *J. Nanomater.*, 2012, **2012**, 891318.

5 P. Mi, F. Wang, N. Nishiyama and H. Cabral, Molecular Cancer Imaging with Polymeric Nanoassemblies: From Tumor Detection to Theranostics, *Macromol. Biosci.*, 2017, **17**(1), 1600305.

6 C. Andreou, Y. Gregoriou, A. Ali and S. Pal, *In vivo imaging with SERS nanoprobes*, 2022, pp. 199–235.

7 J. Fang, H. Nakamura and H. Maeda, The EPR effect: Unique features of tumor blood vessels for drug delivery, factors involved, and limitations and augmentation of the effect, *Adv. Drug Delivery Rev.*, 2011, **63**(3), 136–151.

8 D. Chang, Y. Ma, X. Xu, J. Xie and S. Ju, Stimuli-Responsive Polymeric Nanoplatforms for Cancer Therapy, *Front. Bioeng. Biotechnol.*, 2021, **9**, 707319.

9 Y. Gregoriou, G. Gregoriou, V. Yilmaz, K. Kapnisis, M. Prokopi, A. Anayiotos, K. Strati, N. Dietis, A. I. Constantinou and C. Andreou, Resveratrol loaded polymeric micelles for theranostic targeting of breast cancer cells, *Nanotheranostics*, 2021, **5**(1), 113–124.

10 J. Y. Al-Humaidi, A. A. Nayl, M. M. Abdalla and S. M. Gomha, Synthesis and Biological Activity Evaluation of Some New Coumarin Derivatives as Potent Anticonvulsant and CNS-Depressant Agents, *Polycyclic Aromat. Compd.*, 2022, 2680–2689.

11 C. G. Arya, R. Gondru, Y. P. Li and J. Banothu, Coumarin-benzimidazole hybrids: A review of developments in medicinal chemistry, *Eur. J. Med. Chem.*, 2022, **227**, 113921.

12 M. Kaur, S. Kohli, S. Sandhu, Y. Bansal and G. Bansal, Coumarin: a promising scaffold for anticancer agents, *Anti-Cancer Agents Med. Chem.*, 2015, **15**(8), 1032–1048.

13 A. Thakur, R. Singla and V. Jaitak, Coumarins as anticancer agents: A review on synthetic strategies, mechanism of action and SAR studies, *Eur. J. Med. Chem.*, 2015, **101**, 476–495.

14 G. Wang, S. Sun, B. Wu and J. Liu, Coumarins as Potential Anti-drug Resistant Cancer Agents: A Mini Review, *Curr. Top. Med. Chem.*, 2021, **21**(19), 1725–1736.

15 M. B. Yerer, S. Dayan, M. I. Han, A. Sharma, H. S. Tuli and K. Sak, Nanoformulations of Coumarins and the Hybrid Molecules of Coumarins with Potential Anticancer Effects, *Anti-Cancer Agents Med. Chem.*, 2020, **20**(15), 1797–1816.

16 Q. Yang, S. P. Zhang and Y. Jiang, Studies on a Series of Coumarin Derivatives for Anticancer Activity against Breast Carcinoma Cell Line MCF-7 and Their Molecular Design, *Chin. J. Struct. Chem.*, 2018, **37**(12), 1891–1898.

17 X. Y. Huang, Z. J. Shan, H. L. Zhai, L. Su and X. Y. Zhang, Study on the Anticancer Activity of Coumarin Derivatives by Molecular Modeling, *Chem. Biol. Drug Des.*, 2011, **78**(4), 651–658.

18 S. Sortino, Photoactivated nanomaterials for biomedical release applications, *J. Mater. Chem.*, 2012, **22**(2), 301–318.

19 A. B. Nik, H. Zare, S. Razavi, H. Mohammadi, P. T. Ahmadi, N. Yazdani, M. Bayandori, N. Rabiee and J. I. Mobarakeh, Smart drug delivery: Capping strategies for mesoporous silica nanoparticles, *Microporous Mesoporous Mater.*, 2020, **299**, 110115.

20 B. Reed, *Guidance on the housing and care of zebrafish, Danio rerio*, 2011.

21 C. Collymore, A. Tolwani, C. Lieggi and S. Rasmussen, Efficacy and safety of 5 anesthetics in adult zebrafish (Danio rerio), *J. Am. Assoc. Lab. Anim. Sci.*, 2014, **53**(2), 198–203.

22 C. Collymore, S. Rasmussen and R. J. Tolwani, Gavaging adult zebrafish, *J. Visualized Exp.*, 2013(78), e50691.

23 M. Matthews and Z. M. Varga, Anesthesia and euthanasia in zebrafish, *ILAR J.*, 2012, **53**(2), 192–204.

24 J. D. Clogston and A. K. Patri, Zeta potential measurement, *Methods in molecular biology*, Clifton, N.J., 2011, vol. 697, pp. 63–70.

25 S. B. Sun, P. Liu, F. M. Shao and Q. L. Miao, Formulation and evaluation of PLGA nanoparticles loaded capecitabine for prostate cancer, *Int. J. Clin. Exp. Med.*, 2015, **8**(10), 19670–19681.

26 J. Zong, H. Peng, X. Qing, Z. Fan, W. Xu, X. Du, R. Shi and Y. Zhang, pH-Responsive Pluronic F127-Lenvatinib-Encapsulated Halogenated Boron-Dipyrromethene Nanoparticles for Combined Photodynamic Therapy and Chemotherapy of Liver Cancer, *ACS Omega*, 2021, **6**(18), 12331–12342.

27 G. A. Reynolds and K. H. Drexhage, New Coumarin Dyes with Rigidized Structure for Flashlamp-Pumped Dye Lasers, *Opt. Commun.*, 1975, **13**(3), 222–225.

28 P. K. Makwana, P. N. Jethva and I. Roy, Coumarin 6 and 1,6-diphenyl-1,3,5-hexatriene (DPH) as fluorescent probes to monitor protein aggregation, *Analyst*, 2011, **136**(10), 2161–2167.

29 P. Papageorgis, S. Ozturk, A. W. Lambert, C. M. Neophytou, A. Tzatsos, C. K. Wong, S. Thiagalingam and A. I. Constantinou, Targeting IL13Ralpha2 activates STAT6-TP63 pathway to suppress breast cancer lung metastasis, *Breast Cancer Res.*, 2015, **17**(1), 98.

30 I. Rivolta, A. Panariti, B. Lettiero, S. Sesana, P. Gasco, M. R. Gasco, M. Masserini and G. Miserocchi, Cellular Uptake of

Coumarin-6 as a Model Drug Loaded in Solid Lipid Nanoparticles, *J. Physiol. Pharmacol.*, 2011, **62**(1), 45–53.

31 S. Sakuma, H. Kumagai, M. Shimosato, T. Kitamura, K. Mohri, T. Ikejima, K. Hiwatari, S. Koike, E. Tobita, R. McClure, J. C. Gore and W. Pham, Toxicity studies of coumarin 6-encapsulated polystyrene nanospheres conjugated with peanut agglutinin and poly(N-vinylacetamide) as a colonoscopic imaging agent in rats, *Nanomedicine*, 2015, **11**(5), 1227–1236.

32 G. J. Finn, B. Creaven and D. A. Egan, Study of the in vitro cytotoxic potential of natural and synthetic coumarin derivatives using human normal and neoplastic skin cell lines, *Melanoma Res.*, 2001, **11**(5), 461–467.

33 S. M. Moghimi, A. C. Hunter and T. L. Andresen, Factors Controlling Nanoparticle Pharmacokinetics: An Integrated Analysis and Perspective, *Annu. Rev. Pharmacol. Toxicol.*, 2012, **52**, 481–503.

34 E. V. Batrakova, S. Li, S. V. Vinogradov, V. Y. Alakhov, D. W. Miller and A. V. Kabanov, Mechanism of pluronic effect on P-glycoprotein efflux system in blood-brain barrier: contributions of energy depletion and membrane fluidization, *J. Pharmacol. Exp. Ther.*, 2001, **299**(2), 483–493.

35 N. S. Melik-Nubarov, O. O. Pomaz, T. Dorodnych, G. A. Badun, A. L. Ksenofontov, O. B. Schemchukova and S. A. Arzhakov, Interaction of tumor and normal blood cells with ethylene oxide and propylene oxide block copolymers, *FEBS Lett.*, 1999, **446**(1), 194–198.

36 R. Regev, Y. G. Assaraf and G. D. Eytan, Membrane fluidization by ether, other anesthetics, and certain agents abolishes P-glycoprotein ATPase activity and modulates efflux from multidrug-resistant cells, *Eur. J. Biochem.*, 1999, **259**(1–2), 18–24.

37 E. M. Collnot, C. Baldes, U. F. Schaefer, K. J. Edgar, M. F. Wempe and C. M. Lehr, Vitamin E TPGS P-Glycoprotein Inhibition Mechanism: Influence on Conformational Flexibility, Intracellular ATP Levels, and Role of Time and Site of Access, *Mol. Pharmaceutics*, 2010, **7**(3), 642–651.